PHYSICAL REVIEW B **73**, 075417 (2006)

On the quantum melting of the two-dimensional Wigner crystal

X. Waintal
Nanoelectronics Group, Service de Physique de l'État Condensé, CEA Saclay, 91191 Gif-sur-Yvette cedex, France

(Received 16 September 2005; revised manuscript received 17 November 2005; published 13 February 2006)

The Fermi liquid-Wigner crystal transition in a two-dimensional electronic system is revisited with a focus on the nature of the fixed node approximation done in quantum Monte Carlo calculations. Recently, we proposed [Phys. Rev. Lett. **94**, 046801 (2005)] that for intermediate densities, a hybrid phase (with the symmetry of the crystal but otherwise liquidlike properties) is more stable than both the liquid and the crystal phase. Here we confirm this result both in the thermodynamic and continuum limit. The liquid-hybrid transition takes place at $r_s^* = 31.5 \pm 0.5$. We find that the stability of the hybrid phase with respect to the crystal one is tightly linked to its delocalized nature. We discuss the implications of our results for various transition scenarios (quantum hexatic phase, supersolid, multiple exchange, and microemulsions) as proposed in the literature.

DOI: 10.1103/PhysRevB.73.075417 PACS number(s): 73.20.Qt, 02.70.Ss, 71.10.Ca

I. INTRODUCTION

The competition between electrostatic and kinetic energy in a two-dimensional electron gas is a problem which is simple to formulate (what is the phase diagram of N electrons on a surface S at zero temperature?) yet difficult to tackle. One reason for this difficulty lies in the smallness of the difference in energy between the different phases [the Fermi liquid which is stable at high density when the kinetic energy dominates[1] and the electrostatically favored (Wigner) triangular crystal, stable at low density[2]] compared to the dominant electrostatic energy. In the region of interest in this study, $20 \leqslant r_s \leqslant 80$ (the dimensionless parameter $r_s \propto \sqrt{S/N}$ controls the ratio of the electrostatic energy over the kinetic energy) where there is a strong competition between the two kinds of energy, the difference of energy between the two phases is only of the order of 0.1% of the total energy so that very accurate methods were needed to study this problem. To illustrate the different energy scales, we plot in Fig. 1 the energy of these two phases as a function of $r_s = m^* e^2/(\hbar^2 \epsilon \sqrt{\pi n})$ (e being the electronic charge, ϵ the dielectric constant, m^* the effective mass, and $n = N/S$ the electronic density). At large distances, the physics is entirely electrostatically controlled, and an important amount of energy is involved. Once we add a positive background to the system and make it globally neutral, we arrive at the energies plotted in the upper panel of Fig. 1; on the scale of the plot the liquid and crystal are completely indistinguishable. If we remove the Madelung energy (the excess electrostatic energy of the uniform background with respect to the crystal), we still cannot distinguish between the two phases (see the middle panel of Fig. 1). It is only after we have removed the zero point fluctuation energy of the crystal that the curves become different and show a crossing at $r_s \approx 37$, where the Wigner crystallization has been believed to occur[3,4] (see the lower panel of Fig. 1). The scale of the lower panel of Fig. 1, however, is almost three orders of magnitude smaller than that of the upper panel.

In a seminal article in 1989, Tanatar and Ceperley[3] used a fixed-node quantum Monte Carlo (FN-QMC) technique[5] to locate the critical value $r_s \approx 37 \pm 5$, where the quantum melting of the Wigner crystal occurs. Their work was followed by more precise numerics[6] and a better description of the liquid phase[7,8] that included backflow corrections. On the other hand there were indications that this scenario of a (first-order) direct transition between the Wigner crystal and the Fermi liquid phase might miss some of the physics. For instance, the quantum melting of the bosonic Wigner crystal[9,10] is found (by similar QMC calculations) to occur at $r_s \approx 60$ so that for $37 \leqslant r_s \leqslant 60$ the fermionic statistics (from which all the difficulties of the QMC calculations come, as we shall see) is crucial to stabilize the crystal. Also, the classical melting[11–14] as a function of temperature does not occur in a one step process. The system first loses its translational order but retains some orientational order (hexatic phase[14]) while at a higher temperature, any order disappears. The possibility of an intermediate quantum hexatic phase was put

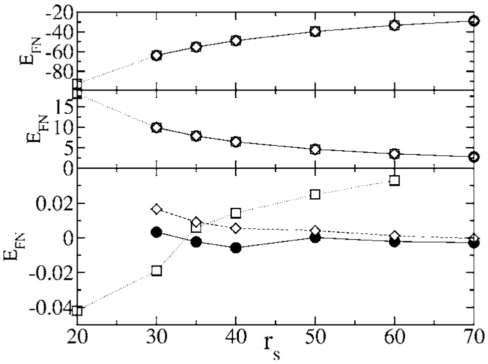

FIG. 1. Quantum Monte Carlo energy as a function of r_s for a system of 56 electrons in 210×208 sites for the liquid phase (squares), solid phase (diamonds), and hybrid phase (full circles). Upper panel: total energy, the three phases are indistinguishable. Middle panel: total energy minus the Madelung (electrostatic) energy $-c_1/r_s$ with $c_1 = 2.2122$. Lower panel: total energy minus the Madelung energy and the energy of the crystal's phonons $c_{1/2} r_s^{-3/2}$ with $c_{1/2} = 1.624$. The energies are given in mRy. For holes in a GaAs heterostructure, a Rydberg corresponds roughly to 350 K ($\epsilon \approx 13\epsilon_0$, $m^* \approx 0.38 m_e$).

forward in Refs. 15,16. In fact, it was recently argued on rather general grounds, that a direct first order transition is simply impossible in this system[17,18] but should occur through a series of intermediate phases (including bubbles or stripes of one phase in the other). The possibility of a supersolid phase analogous to the one proposed by Andreev and Lifshitz[19] has also been considered.[20–22] All these indications[23] led us recently to revisit the melting of the Wigner crystal in the framework of the FN-QMC calculations. We considered a third phase called hybrid phase (as it had the symmetry of the crystal but is otherwise delocalized) and showed that it was more stable than both the liquid and crystal phases (full circles in the lower panel of Fig. 1) in the intermediate density range[24] giving strong support to the more exotic scenarios.

To understand the status of our result, however, it is of prime importance to understand the nature of the fixed-node (FN) approximation involved in the FN-QMC technique. In practice, the FN-QMC algorithm is fed with a wave function called the *guiding wave function* (GWF) that has to be given explicitly, and that should be as close as possible to the ground state of the system. The FN-QMC algorithm projects the GWF onto the (true) ground state of the system. However, to avoid the notorious sign problem that arises in QMC simulations involving fermions, one approximation is introduced; the projection is done with the constraint that *the sign of the wave function (nodal structure) remains unchanged* at every point of the Hilbert space. The method gives the best wave function for a given structure of the nodes of the GWF and is in this sense variational.[25] The physical meaning of the FN approximation is not completely obvious. Implicit in the interpretation given above of the FN-QMC results is that a GWF is associated to a phase (crystal, liquid, or hybrid) the stability of which can therefore be studied. However, this paradigm should not be taken too literally and will be made more precise in this article.

After presenting our model and the FN-QMC method in Sec. II, we perform FN-QMC calculations on a small system of four electrons (Sec. III). As this system can be studied exactly, it is an interesting tool to study the nature of the FN approximation. We find that in addition to the FN results at a large imaginary (projection) time, important information is embedded in the evolution of the results from the variational calculation to the full FN-QMC results. In Sec. IV, we explain the construction of the hybrid GWF, and show that its nodal structure corresponds to delocalized waves. Section V is devoted to a characterization of the physics associated with the hybrid GWF. This is done through a systematic study of various physical quantities, and in particular of their evolution between the variational and FN-QMC calculations. We find that the success of the hybrid GWF with respect to the crystal one is closely linked to its delocalized nature. Section VI contains a detailed discussion of various technical aspects (thermodynamic limit, lattice effects, mixed, and unbiased estimates,…). The chief result of Sec. VI is a precise determination of the critical value $r_s^*=31.5\pm0.5$. at which the liquid-hybrid transition takes place (in both the continuum and thermodynamic limits). In Sec. VII, we discuss the implications of our results to the scenarios proposed in the literature.

II. MODEL AND METHOD

A. System under consideration

The system under consideration consists of N spinless electrons on a rectangular $L_x\times L_y$ grid with nearest-neighbor hopping and long-range Coulomb repulsion. To avoid strong finite-size effects on the electrostatic energy, the system is repeated periodically and fills the whole two-dimensional (2D) plane. In practice, we use periodic boundary conditions for the hopping terms and the effective two-body interaction is obtained from the bare Coulomb interaction using the Ewald summation technique. The system Hamiltonian reads[26]

$$H=-t\sum_{\langle\vec r,\vec r'\rangle}c^\dagger_{\vec r}c_{\vec r'}+\frac{U}{2}\sum_{\vec r\neq\vec r'}V(\vec r-\vec r')n_{\vec r}n_{\vec r'}+\lambda, \tag{1}$$

where the operator $c^\dagger_{\vec r}$ ($c_{\vec r}$) creates (destroys) an electron on point $\vec r$ with the standard anticommutation relation rules, the sum $\Sigma_{\langle\vec r,\vec r'\rangle}$ is done on the nearest-neighbor points on the grid and t is the corresponding hopping amplitude. The density operator reads $n_{\vec r}=c^\dagger_{\vec r}c_{\vec r}$. U is the effective strength of the two body interaction $V(\vec r)$ which reads

$$V(\vec r)=\sum_{\vec L}\frac{1}{|\vec r+\vec L|}\operatorname{erfc}(k_c|\vec r+\vec L|)+\frac{2\pi}{L_xL_y}\sum_{\vec K\neq\vec 0}\frac{1}{|\vec K|}\operatorname{erfc}[|\vec K|/(2k_c)]\cos(\vec K\cdot\vec r). \tag{2}$$

In the previous equation, k_c is a(n) (irrelevant) cutoff. The vector $\vec L$ takes discrete values $\vec L=(n_xL_x,n_yL_y)$ with n_x and n_y integer numbers. The vector $\vec K$ also takes discrete values, $\vec K=[(2\pi/L_x)n_x,(2\pi/L_y)n_y]$ and $(n_x,n_y)\neq(0,0)$. The complementary error function is defined as $\operatorname{erfc}(r)=(2/\sqrt{\pi})\int_x^\infty e^{-t^2}dt$. In order to assure electrostatic neutrality we add a positive continuum background

$$\lambda/N=4t+U\tilde V(\vec 0)-2U\nu\sqrt{\pi}/k_c-2Uk_c/\sqrt{\pi}, \tag{3}$$

where $\nu=N/(L_xL_y)$ is the average number of electrons per site and $\tilde V(\vec r)=V(\vec r)$ with the restriction that the sum over $\vec L$ does not includes the null vector.

The presence of the grid can be understood either as a discretization of the continuum problem (and the nearest-neighbor hopping corresponds to the discretized Laplacian) or as a tight-binding approach to two-dimensional electron systems, where each site corresponds to an atomic orbital. In conventional 2D systems (say GaAs/GaAlAs heterostructures), densities range from $n_s\approx10^{12}\ \mathrm{cm}^{-2}$ down to $n_s\approx10^{10}\ \mathrm{cm}^{-2}$. Since the distance between nearest atoms is of the order of a few Angstroms, this would lead to $\nu\sim10^{-4}$ to $\nu\sim10^{-2}$ electrons per site in our tight-binding picture. In this study, we will study systems with $\nu=1/56$, $\nu=1/224$, and $\nu=1/780$ close to realistic values.

The presence of the jellium (which is merely a constant term and thus cannot affect the physics) allows us to make a quantitative contact with the literature in the continuum limit as $\nu\to0$. In this limit, the physics depends only on the r_s

parameter which reads, $r_s=U/(2t\sqrt{\pi\nu})$ while the Rydberg unit of energy is $Ry=U^2/(4t)$. In the following, unless specifically stated, we shall measure all energies E in the unit of $2\pi N\nu t$ (i.e., the energy per particle in a unit of the Fermi energy of the noninteracting problem). With this normalization, the energy of the system at $r_s=0$ in the thermodynamic $N\gg 1$ and continuum $\nu\ll 1$ limit is $E=1$ so that results in Rydberg can be obtained by multiplying the energies (in the unit of $2\pi N\nu t$) by $2/r_s^2$.

We have added a(n) ("infinitely") small disorder $\Sigma_{\vec{r}} v_{\vec{r}} n_{\vec{r}}$ in order to lift the degeneracies of the noninteracting problem and allow the translational symmetry breaking of the crystal. $v_{\vec{r}}$ are independent and uniformly distributed inside $[-W/2,+W/2]$. We chose $W=10^{-3}$ corresponding to an extremely large ratio $l/\lambda_F=96\nu t^2/W^2\sim 10^6$ of the mean-free-path l over the Fermi wavelength λ_F. The correction to the energy due to the disorder is smaller than our statistical accuracy and we explicitly checked that our result is insensitive to the disorder presence.

The grid has been chosen to accommodate a(n) (almost) triangular Wigner crystal without distortion. Hence we use systems of $N=Q\times R$ electrons [R (R even) lines of Q particles] in $Qd_x\times Rd_y$ sites. The triangular crystal requires $d_y/d_x=\sqrt{3}/2\approx 0.866$. In this work, we focus on $d_y/d_x=14/16\approx 0.875$ and $d_y/d_x=26/30\approx 0.866$ for which we find that the distortion is negligible.

B. The Green function Monte Carlo method in the fixed–node approximation

We aim to sample the ground state $|\Psi_0\rangle$ of H and its corresponding ground-state energy E_0 with the Green function Monte Carlo (GFMC) technique. The idea behind this method is to project an initial (variational) guiding wave function $|\Psi_G\rangle$ on the exact ground state $|\Psi_0\rangle$ by applying the operator $e^{-H\beta}$ in a stochastic way, with a large imaginary time β. In practice, one works in the many particle basis $R=(\vec{r}_1,\vec{r}_2\ldots\vec{r}_N)$ and applies the function

$$G_{R'R}=\delta_{R'R}-\tau\Psi_G(R')[H_{R'R}-\omega\delta_{R'R}]\Psi_G^{-1}(R), \qquad (4)$$

where $\Psi_G(R)=\langle R|\Psi_G\rangle$, τ is a (small) time step, and ω is an unimportant offset of the energies (that should be roughly set to the ground state energy of the system, here we took $\omega/(2\pi\nu t)=1-r_s$). In the absence of the $\Psi_G(R)$, G is a discretized version of the operator $e^{-H\beta}$ for a small (imaginary) time step τ. Upon applying $n=\beta/\tau$ times G on a vector $\Psi_G^2(R)$, the $\Psi_G(R')$ on the left of Eq. (4) are canceled by the $\Psi_G^{-1}(R)$ on the right so that one obtains

$$I_n=\sum_{R'R}(G^n)_{R'R}\Psi_G^2(R)=\langle\Psi_G|e^{-(H-\omega)n\tau}|\Psi_G\rangle \qquad (5)$$

from which one can extract the ground state energy (as $I_{n+1}=e^{-(E_0-\omega)\tau}I_n$ when $\beta=n\tau\to\infty$).

The stochastic implementation of this scheme is based on the Green function Monte Carlo for lattice Hamiltonians introduced in Ref. 26 to which we refer for more details. The algorithm to update the Slater determinants used in the calculation of $\Psi_G(R)/\Psi_G(R')$ can be found in Ref. 27. By sampling directly the time spent by the walkers at one point of the Hilbert space using the algorithm described in Ref. 26 we can use arbitrary small time steps τ without any loss in computing time and hence effectively work in continuum (imaginary) time. Instead of using the standard branching technique, the control of the walkers population is done using a fixed number of walkers and the reconfiguration algorithm introduced by Sorella.[28] This algorithm allows one to avoid the bias introduced in the branching technique by artificially controlling the walker population. Quantum averages of physical quantities $\langle\cdots\rangle$ are calculated using the forward walking technique,[28] and hence do not suffer from the bias of mixed estimates.

So far the scheme is essentially exact. However, it suffers from the usual "sign problem," the sign of $G_{R'R}$ fluctuates so that the statistical accuracy decreases exponentially with β, and it is of little practical use. One way out of the sign problem is the fixed-node approximation, where one forbids the sign of the wave function to change upon applying G [hence the name; the nodal surface where the wave function changes of sign remains the same than the one of $\Psi_G(R)$]. The practical implementation of the fixed-node approximation on a grid is done[25] by replacing H by an effective Hamiltonian H^{FN} that depends on the GWF. $H^{\mathrm{FN}}_{R'R}$ is equal to $H_{R'R}$ when $G_{R'R}>0$. When $G_{R'R}<0$, the link is cut $H^{\mathrm{FN}}_{R'R}=0$ and is replaced by an effective potential $H^{\mathrm{FN}}_{RR}=H_{RR}+\Sigma_{R'}\theta(-G_{R'R})\Psi_G(R')H_{R'R}\Psi_G^{-1}(R)$, where $\theta(x)$ is the Heaviside function [this corresponds to replace the value of the wave function on those sites R' by the surmise $\Psi_G(R')$]. The fixed-node approximation can be thought of as a "supervariational" technique, where the amplitude of the wave function is optimized at every point of the Hilbert space while its sign remain fixed. It can be proved indeed that the energies E_{FN} calculated with H_{FN} are larger than the true ground-state energy E_0 but smaller than the variational energy associated with the guiding wave function.[25] The fixed-node approximation in a lattice looks *a priori* more drastic than in the continuum since we do impose the ratio of the wave function across the nodal surface. However, for $\nu\ll 1$ the fraction of "nodal" sites goes to zero and the technique becomes equivalent to the fixed node diffusive Monte Carlo used in the continuum.[3]

As an illustration, we present in Fig. 2 a typical trace obtained for 32 particles at $r_s=40$. $E_{\mathrm{FN}}(\beta=0)$ corresponds to the variational energy $\langle\Psi_G|H|\Psi_G\rangle/\langle\Psi_G|\Psi_G\rangle$. After an initial rapid decrease, the FN energy (per particle) $E_{\mathrm{FN}}(\beta)$ decreases slowly as $1/\beta$ (see inset) and then saturates above an imaginary time $\beta_{\mathrm{sat}}\propto 1/(\nu t)$. The energy is estimated by further averaging the result over β for $\beta>\beta_{\mathrm{sat}}$. In the rest of this paper, unless explicitly stated, the obtained accuracy for $E_{\mathrm{FN}}(\beta)$ is ± 0.002 or better while the precision on quantities other than the energy will be of the order of the size of the symbols. This remarkable precision (here the relative accuracy is $\sim 10^{-5}$) should be contrasted with the fact that important changes in the physics can lead to very tiny changes in energy. For instance the condensation energy of a superconductor[29] (the difference of energy between the superconducting and the normal state) is only a very small fraction $\sim(\Delta/E_F)^2\sim 10^{-6}$ (Δ is the superconducting gap, E_F

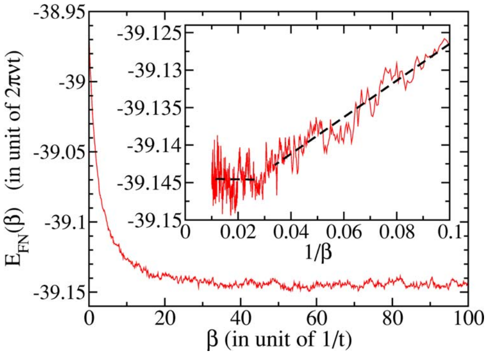

FIG. 2. (Color online) Typical curve of $E_{\text{FN}}(\beta)$ as a function of β. A system of 32 particles in 64×112 sites at $r_s=40$ for a liquid GWF with $A=4.5$. Here, 8.10^5 walkers were used, $\omega=-39$ and $\tau=10^{-5}/t$. Inset: the same curve as a function of $1/\beta$. The dashed lines are linear fits to guide the eye.

the Fermi energy) of the total energy (only electrons near the Fermi surface form Cooper pairs). The formation of a Wigner crystal (localized in real space) from a Fermi liquid (localized in momentum space) corresponds however, to a complete reorganization of the system and the changes in energy, though small ~ 0.01, can be measured with the GFMC technique.

C. Guiding wave functions

Central in the fixed-node technique is the choice of the GWFs used in the calculations. Here, the guiding wave functions have the general form of a Slater determinant multiplied by a Jastrow function,

$$\Psi_G(R) = \text{Det}[\phi_i(\vec{r}_j)] \times \prod_{i<j} J(|\vec{r}_i - \vec{r}_j|). \tag{6}$$

The Jastrow part takes Coulomb interaction into account by introducing the correlations between electrons. Since it has no nodes, the FN results should not depend on its particular form (as we explicitly checked). We use modified Yukawa functions,[30]

$$J(r) = \exp\left[\frac{aA(r_s)}{r}(1 - e^{-B(r_s)r/a})\right], \tag{7}$$

where $a=1/\sqrt{\pi\nu}$ is the average distance between electrons. $A(r_s)$ and $B(r_s)$ are (optimized) variational parameters. To avoid the Coulomb singularity when two electrons get close to each other, we impose the cusp condition[5] that reads $B=\sqrt{r_s/A}$ for the modified Yukawa.

The Slater determinant of one-body wave functions, $\text{Det}[\phi_i(\vec{r}_j)]$ enforces the antisymmetric nature of the fermionic wave function and is responsible for the nodal structure of the GWF. The GWF used in the literature for the study of the melting of the Wigner crystal[3,6] are of two kind, adapted to the two limits of very low (large) r_s;

(i) For the liquid state the GWF Ψ_{liq} is constructed out of plane waves $\phi_i(\vec{r}_j) \propto e^{i\vec{k}_i\cdot\vec{r}_j}$ with a well-defined Fermi surface. Ψ_{liq} is the exact ground state at $r_s=0$.

(ii) For the crystal GWF Ψ_{cry}, localized orbitals $\phi_i(\vec{r}_j) \propto e^{-(\vec{r}_j-\vec{u}_i)^2/(2d_0^2)}$ are used. Here the $\vec{u}_i$ with $i\in\{1\cdots N\}$ stand for the positions of the electrons in the classical crystal. Ψ_{cry} provides the exact ground state in the continuum at large r_s with the variational parameter $d_0 \propto a/r_s^{1/4}$. This GWF captures the two leading terms of the large r_s expansion of the energy (Madelung and zero point fluctuation energy) that reads,

$$E = -c_1 r_s/2 + c_{1/2}\sqrt{r_s}/2 + \cdots \tag{8}$$

with $c_1=2.2122$ and $c_{1/2}=1.624$.

In this paper, we will use the two previously mentioned GWF, and a third (hybrid) one that somehow interpolates between the crystal (real space) and the liquid (momentum space).

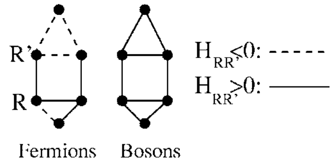

FIG. 3. A schematic view of Eq. (9). The circles symbolize sites R in Hilbert space and the full (dashed) lines positive (negative) off-diagonal matrix elements $H_{RR'}$. The corresponding lattice is frustrated for fermions.

III. THE SIGN PROBLEM AND THE FIXED-NODE APPROXIMATION

In this section, we come back to the sign problem, and investigate the nature of the approximation involved in the fixed-node approximation. One way to understand the sign problem is to consider it as a frustration problem in Hilbert space; we seek to solve the Schrödinger equation which formally reads in R space,

$$\sum_{R'} H_{RR'}\Psi_0(R') = E_0\Psi_0(R). \tag{9}$$

Two-body interactions and external potentials are diagonal in the R space and H_{RR} can always be considered to be positive (by shifting H by a constant). The off-diagonal elements $H_{RR'}$ come from kinetic energy. They are positive for bosons but are alternatively positive and negative for fermions as shown schematically in Fig. 3. The bosonic case does not suffer from any sign problem and $\Psi_0^{\text{boson}}(R)$ can be found efficiently. We now consider a fictitious Ising model, where an Ising variable $s(R)=\pm 1$ is placed on each site R of the Hilbert space and is coupled to its neighbors by a coupling $H_{RR'}$ (which can be ferromagnetic or antiferromagnetic). If this fictitious model had no frustration, then its ground state $s_0(R)=\pm 1$ could be trivially found and one can easily verify that $\Psi_0^{\text{fermion}}(R)=s_0(R)\Psi_0^{\text{boson}}(R)$ would be the exact ground state of the fermionic problem. Hence the sign problem arises from the frustrated nature of Eq. (9). From this point of view, the fixed-node approximation consists in cutting some links of this fictitious Ising model so that it is no longer frustrated and admits $s_0(R)=\text{sgn}[\Psi_G(R)]$ as its ground state. The FN approximation does not have a simple physical meaning and thus seems difficult to control.

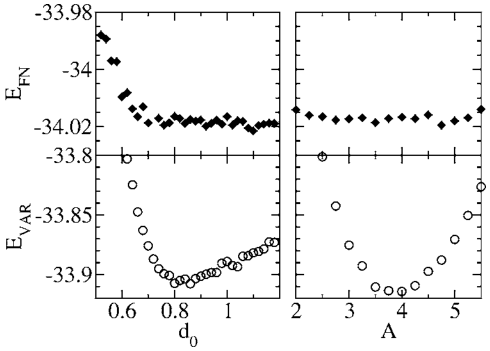

FIG. 4. Comparison between the fixed-node E_{FN} (upper panels) and variational E_{VAR} (lower panels) energies as a function of d_0 (left panels, d_0 in unit of a) and A (right panel) for a system of 30 particles in 40×42 sites at $r_s=35$ using the Ψ_{cry} GWF. Left panels: $A=4.5$. Right panels: $d_0=0.76a$.

In Fig. 4, we compare the FN results with the variational (i.e., $\beta=0$) results for a system of 30 particles at $r_s=35$. The calculations have been done for the Ψ_{cry} GWF so that we can compare the influence of the two parameters d_0 and A. While d_0 enters in the definition of the Slater determinant and hence of the nodal structure, A defines the Jastrow part which does not change sign and (in the limit $\nu \ll 1$) the FN results should thus be insensitive to the choice of A. On the right panel of Fig. 4, we see that it is indeed the case. The function $E_{\mathrm{FN}}(A)$ is flat at the precision of the calculation (± 0.002 here) while the variational energy $E_{\mathrm{VAR}}(A)$ shows a pronounced minimum at $A\approx 4$. On the left panels of Fig. 4, we plot E_{FN} and E_{VAR} as a function of d_0. One would expect the two curves to present a minimum at the same value of d_0 (which is what is usually assumed, the FN calculations being done in most cases with parameters optimized at the variational level). However, one observes that for $d_0 \geqslant 0.8$ (variational minimum) the FN energy is flat upon increasing d_0. Hence, the nature of the approximation done in a fixed-node calculation is not simply related to the original variational wave function used for fixing the nodal surface, and the method can potentially capture more physics than originally thought.

To gain further insight, we now discuss the instructive example of four electrons in a 6×8 grid. This system is small enough (the size of the Hilbert space is $\sim 2.10^5$) so that its ground state can be found exactly using the Lancsos algorithm and compared with the result of a fixed-node calculation. We introduce the density $\rho(\vec{r})$ and density-density correlation function $g(\vec{r})$,

$$\rho(\vec{r}) = \frac{1}{N}\langle c^{\dagger}_{\vec{r}} c_{\vec{r}}\rangle, \tag{10}$$

$$g(\vec{r}) = \frac{L_x L_y}{N(N-1)} \sum_{\vec{h}} \langle c^{\dagger}_{\vec{r}+\vec{h}} c^{\dagger}_{\vec{h}} c_{\vec{h}} c_{\vec{r}+\vec{h}}\rangle, \tag{11}$$

which measures, respectively, the average number of electrons on site $\vec{r}$ and the probability to find an electron on site $\vec{r}$ knowing that there is one particle on site $\vec{0}$ (both are normalized to one). From these two quantities, we define the participation ratio

$$\rho_2 = 1 \Bigg/ \left[L_x L_y \sum_{\vec{r}} \rho^2(\vec{r})\right], \tag{12}$$

which roughly measures the number of occupied sites in the ground states (ρ_2 interpolates from 1 to ν as r_s goes from 0 to ∞) and the "rigidity" parameter g_2,

$$g_2 = \frac{1}{L_x L_y} \sum_{\vec{r}} [g(\vec{r}) - 1]^2. \tag{13}$$

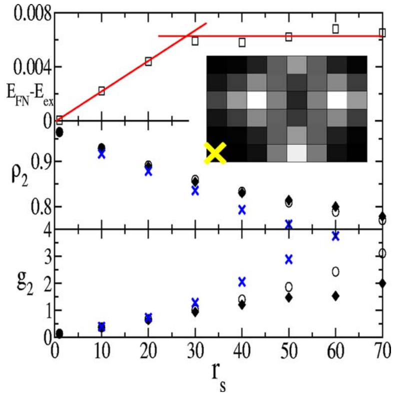

FIG. 5. (Color online) Comparison between the fixed-node calculation with a liquid GWF and the exact result for a system of four particles in 8×6 sites. Upper panel: the difference between the FN and exact energy. The lines are a guide to the eye. Middle panel: the participation ratio per site ρ_2 for the exact (empty circles) FN (full diamonds) and variational (crosses) calculation. Lower panel: idem for the rigidity parameter g_2. Inset: the exact density-density correlation function $g(\vec{r})$ at $r_s=20$. $g(\vec{r})$ measures the probability to find a particle on site $\vec{r}$ knowing that one particle is on site $\vec{0}$ indicated by the cross in the corner of the sample. The gray scale range from 0 (black) to 3 (white).

The comparison between the exact result and the FN calculation is presented in Fig. 5. In the inset of Fig. 5, we show the exact $g(\vec{r})$ at $r_s=20$. $g(\vec{r})$ has three well-defined maxima at the positions of the classical Wigner crystal. Upon increasing r_s, the system gets more and more crystal-like and these maxima become more pronounced which leads to an increase of g_2 (lower panel) and a decrease of ρ_2 (middle panel). Figure 5 shows two regimes. For $r_s \leqslant 30$, the error on the energy (upper panel) increases linearly while the two other physical quantities ρ_2 and g_2 are in very good agreement with the exact result. Hence the FN result, though calculated with a liquid GWF made of plane waves, is well able to reproduce the ground state of a system which (at $r_s=30$) is really crystal-like. Above $r_s \geqslant 30$ the error saturates to 0.007, ρ_2 is still in good agreement with the exact result, but the error on g_2 starts to increase significantly. At $r_s=70$, the error on the energy is only 0.01% of the total energy ($E_0\approx 1-r_s$) while the error on g_2 is much larger $\sim 33\%$.

Hence the FN approximation provides a very good description of the ground state up to a rather large value of r_s (here around 30) even though the system is very crystal-like and we started from a liquid GWF. It also provides a good quantitative value of the energy even for higher values of r_s, where the FN approximation no longer accurately describes the physics. Maybe even more importantly, Fig. 5 gives us a clue on how to control the FN approximation; we find that when the FN approximation starts to fail ($r_s \approx 30$), the difference between the FN results and the variational results starts to increase drastically. In addition, the FN results (here for ρ_2 and g_2) lies in between the variational and the exact results so that the fixed-nodal surface can be viewed as a "wall" preventing the system from relaxing to the true ground state. Hence some information on the nature of the ground state can be extracted from the evolution of the physical quantities between the variational and the FN estimates (and not only from the study of the FN quantities alone). This idea will be put to application in Sec. V by looking at how the physics in the various GWF is amplified or washed out by the FN projection.

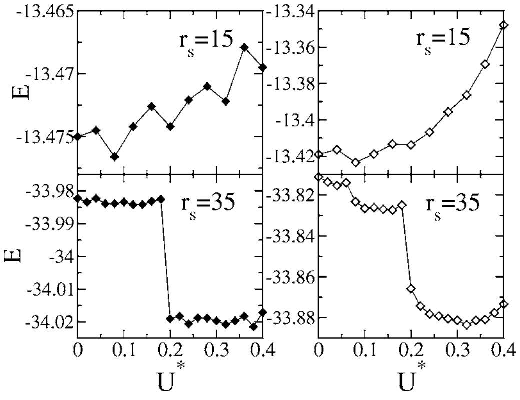

FIG. 6. The fixed-node energy (left panels) and variational energy (right panels) at $r_s=15$ (upper panels) and $r_s=35$ (lower panels) as a function of U^*. The system contains 30 particles in 40×42 sites and the calculations are done with the hybrid GWF.

IV. CONSTRUCTION OF A HYBRID PHASE

The melting point of the Wigner crystal can be viewed as the point above which the problem is well described in real space (crystal with particles at given positions) and below which the momentum space is to be used (liquid with a well-defined Fermi surface). Hence, the melting point itself is somehow the point of "maximum uncertainty," where the problem is equally badly described in both momentum and real space representation. In the standard scenario of a (first-order) direct transition between the liquid and the crystal, this point is nothing else than the point where the energy of one state crosses the other one. Here, we consider another scenario which interpolates between momentum and real space. In order to do so, we considered in Ref. 24 a GWF, we called a hybrid GWF aimed to provide such an interpolation. As we have seen, we find that this hybrid GWF provides the lowest energy in the intermediate region of r_s.

The construction of the hybrid GWF $\Psi_{\rm hyb}$ is done in such a way that the resulting $\phi_i(\vec{r}_j)$ are the Bloch states of electrons in a triangular crystal. First, an effective one-body Hamiltonian $H_{\rm eff}$ is constructed for an electron in an *attractive* periodic potential that has the symmetry of the classical (triangular) Wigner crystal,

$$H_{\rm eff} = -t \sum_{\langle \vec{r},\vec{r}'\rangle} c^{\dagger}_{\vec{r}} c_{\vec{r}'} - U^* \sum_{\vec{r}} W(\vec{r}) n_{\vec{r}}, \qquad (14)$$

where the one-body potential is $W(\vec{r})=\Sigma_{i=1}^{N} V(\vec{r}-\vec{u}_i)$. The singularity of $W(\vec{r})$ at the position of the classical crystal $\vec{r}=\vec{u}_i$ has been removed by setting $W(\vec{u}_i)\equiv W[\vec{u}_i+(1,0)]$ [we checked that other choices of $W(\vec{r})$ give consistent results]. In a second step, $H_{\rm eff}$ is numerically diagonalized using the Lanczos algorithm. The N orbitals of lowest energy $\phi_i(\vec{r})$ $(1\leqslant i\leqslant N)$ are then used to construct the Slater determinant. *A priori* U^* is a variational parameter that allows for an interpolation between $\Psi_{\rm liq}$ (at $U^*=0$) and localized orbitals leading to a GWF similar to $\Psi_{\rm cry}$ (at $U^*\gg 1$).

In Fig. 6, we plot the energy as a function of U^* for two values of r_s below ($r_s=15$ upper panels) and above ($r_s=35$ lower panels) the expected liquid-crystal transition (which is found around $r_s\approx 20-25$ for this system of 30 particles in 40×42 sites). At $r_s=15$ the energy increases with U^* indicating that the free-plane-wave solution provides the best nodal structure. The increase of the fixed-node energy (left panels) is however 10 times smaller than the increase of the variational energy and is only slightly above the statistical resolution. At $r_s=35$, the situation is completely changed, and the FN energy shows a sharp drop around a particular critical value $U^*=U^*_C\approx 0.2$. This point corresponds, as we shall see, to the value of U^* above which the GWF has the symmetry of the crystal. We find that the fixed-node energy is completely flat above and below this threshold, indicating that the drop in energy is really associated to the change of symmetry.

More insight on the significance of the critical value U^*_C can be found by looking at the eigenenergies ϵ_i associated with the orbitals $\phi_i(\vec{r})$. The lowest values of these energies ϵ_i (which have no physical meaning by themselves and are just a convenient way to get information on the orbitals) are plotted in the upper panel of Fig. 7 as a function of U^*. At $U^*=0$ they form one unique band with a parabolic dispersion $\epsilon_i\propto k_i^2$. At $U^*\gg 1$, the periodic potential is at the origin of a more complex band structure, and the band of lowest energy (which contains exactly N levels) detaches from the rest of the spectrum and becomes narrower as U^* increases. What is important here is that the point where this band of lowest energy separates from the rest of the level (see Fig. 7, upper panel) corresponds exactly to the point where the energy has a drop (see Fig. 7, lower panel). Above this point, Bloch theory tells us that the $\phi_i(\vec{r})$ can be written in terms of the Bloch waves of one band only;

$$\phi_i(\vec{r}) = u_{\vec{k}_i}(\vec{r}) e^{i\vec{k}_i\cdot\vec{r}}, \qquad (15)$$

where $u_{\vec{k}_i}(\vec{r})$ is a function with the periodicity of the crystal and the momentum have their value within the first Brillouin zone of the triangular lattice, i.e., a hexagonal Fermi surface. In that sense, the hybrid GWF is liquidlike (made of plane waves) with the triangular symmetry. However, since the only thing that enters in the GWF is actually the determinant,

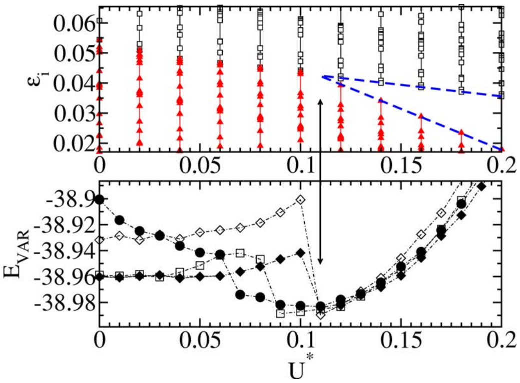

FIG. 7. (Color online) Upper panel: the lowest energy levels ϵ_i of the fictitious one-body problem H_{eff} as a function of the variational parameter U^* for a system of 72 particles in 96×168 sites. The 72 first energies ("one full band" at large U^*) are shown as triangles while the higher values of ϵ_i are shown as squares. The dashed lines correspond to the 72th and 73th values of ϵ_i. They indicate the critical value $U_c^*\approx0.12$, where the band of lowest energy splits from the rest of the fictitious spectrum. Lower panel: the variational energy as a function of U^* for $2P^2$ particles in $16P\times28P$ sites at $r_s=40$ with $A=4.5$. $P=3$ (empty diamonds), $P=4$ (empty squares), $P=5$ (full circles), and $P=6$ (full diamonds).

$\det[\phi_i(\vec{r})]$, it is equivalent to use [instead of Eq. (15)] linear combinations of the Bloch waves, leading to the so-called Wannier functions,

$$\phi_i(\vec{r}) = F(\vec{r}-\vec{u}_j) \text{ with } F(\vec{r}) \equiv \sum_i u_{\vec{k}_i}(\vec{r})e^{i\vec{k}_i\cdot\vec{r}}. \tag{16}$$

Writing the $\phi_i(\vec{r})$ in the form of Eq. (16), the hybrid GWF looks similar to the crystal one [for which $F(\vec{r})$ takes the form of a Gaussian function]. The Wannier functions are not uniquely defined [since $u_{\vec{k}_i}(\vec{r})$ is defined up to an arbitrary phase] and an important effort has been done in the literature (in the context of *ab initio* electronic structure calculation mostly) to define the maximally localized Wannier functions. The fundamental result for us is[31,32] that *at* $U^*=U_C^*$, $F(\vec{r})$ *cannot decrease faster than algebrically with* $\vec{r}$ and is hence a delocalized function over the sample. This is in sharp contrast with the crystal GWF for which the $\phi_i(\vec{r})$ are strongly localized around the classical positions $\vec{u}_i$ of the crystal. For $U^*\gg U_C^*$, the lowest band becomes narrower, and an exponentially localized Wannier function $F(\vec{r})\sim e^{-hr}$ can be constructed. However, the point of interest for us is $U^*\approx U_C^*$, where the drop in energy occurs. In the rest of this paper, we will stick to this value (i.e., U^* is set to a value just above the point where the splitting of the bands occurs) where the Wannier functions are delocalized and hence completely different from the crystal GWF at a qualitative level. The Jastrow function for the hybrid GWF is taken to be the same as the liquid one (We checked that taking the crystal Jastrow or optimizing the Jastrow parameter A especially for the hybrid GWF did not affect the results).

V. CHARACTERIZATION OF THE HYBRID PHASE

As we have seen in the Introduction (as shown in the lower panel of Fig. 1), the hybrid GWF provides the lowest energy for a rather large domain of r_s. Having established that, we now try to understand the physical origin of this success and the nature of the corresponding phase. From the construction of the hybrid GWF (a Slater determinant made of a *delocalized* Wannier function), we expect (at the variational level) something somewhere between the crystal (it has its triangular symmetry) and the liquid (it is made of delocalized one-body functions). While the crystal aspect is straightforward, the characterization of the liquid aspect is a difficult task within the FN-QMC. Indeed, the FN-QMC method mainly provides access to quantities [like $\rho(\vec{r})$ or $g(\vec{r})$] which are diagonal in the real space representation, and hence not very likely to characterize the liquid behavior.

In Ref. 24, we studied some physical quantities for the three GWF with the implicit idea that these quantities would characterize the phase associated with each GWF. Here we follow a different approach. Following the insight we obtained in Sec. III on a small system, we study how the physical quantities evolve between the variational value $O_{\text{VAR}}=\langle\Psi_G|O|\Psi_G\rangle$ and the FN results $O_{\text{FN}}=\langle\Psi_0^{\text{FN}}|O|\Psi_0^{\text{FN}}\rangle$, as this gives the general trend toward the true ground state of the system. The different GWFs capture different physics, which can be either amplified or washed out by the FN projection procedure, giving hints on the true nature of the ground state.

In the right panel of Fig. 8 we plot the kinetic and interaction energies as a function of r_s. The variational values of the hybrid GWF are in the middle of those obtained with the liquid and crystal GWF. Upon applying the FN projector $e^{-\beta H^{\text{FN}}}$ on the hybrid (and crystal) GWF, the value of the kinetic energy decreases and converges to a value rather close to the variational kinetic energy of the liquid. It is important to note that these differences in (kinetic or interaction) energy are about 5 to 10 times bigger than the differences observed on the total energy. This decrease of the kinetic energy to an almost liquid value is a strong sign of the delocalized nature of the ground state. As r_s increased, however, this tendency also diminishes. This delocalization can also be seen indirectly on the electronic density $\rho(\vec{r})$. An example of $\rho(\vec{r})$ is shown in the upper panel of Fig. 9. At first sight the density looks crystal-like (strong peaks forming a triangular lattice). However, the height of the peaks ($\rho_{\max}$ as shown in the lower left panel of Fig. 8) and the depth of the valleys ($\rho_{\min}$ as shown in the upper left panel of Fig. 8) show not only that these peaks are not very pronounced (at $r_s=32$, the density at the peaks is only twice the average density while the "background" contains $\rho_{\min}\approx35\%$ of the electrons) but also that the contrast tends to diminish from the variational to the FN estimate (especially for the crystal GWF). Similar conclusions can be drawn from the density-density correlation function $g(\vec{r})$ (a three-dimensional plot is shown in Fig. 9. Figure 10 gives a cross section.) For $r_s=35$ (the upper panel of Fig. 10) the peaks of both the hybrid and crystal results tend to be washed out after the FN projection. At $r_s=60$, however (lower panel of Fig. 10) the tendency is inversed and the hybrid result tends to get more localized when going from variational to the FN results (the same thing can be seen on $\rho_{\max}$, see the lower left panel of Fig. 8).

All the physical quantities discussed above indicate the same tendency: at the variational level the hybrid GWF lies

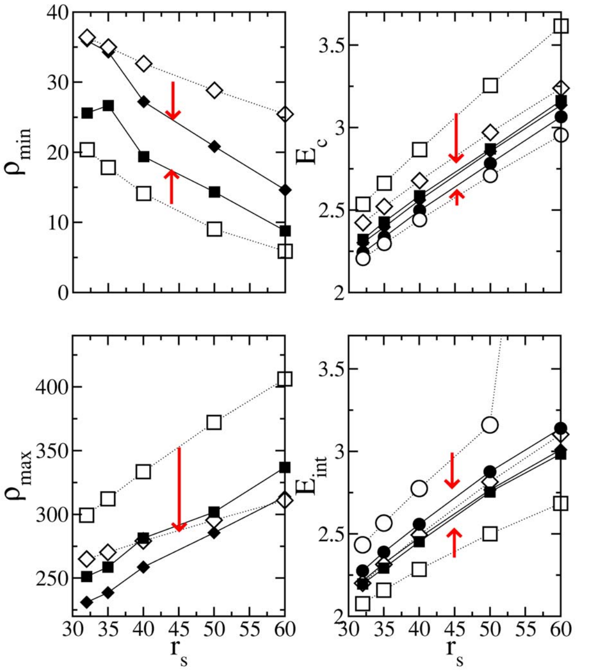

FIG. 8. (Color online) Evolution from variational to FN results for various physical quantities. $\rho_{\min}(r_s)=\min_{\vec{r}}\,\rho(\vec{r})$ (upper left panel), $\rho_{\max}(r_s)=\max_{\vec{r}}\,\rho(\vec{r})$ (lower left panel), $E_c(r_s)$ (upper right panel), and $E_{\rm int}(r_s)$ (lower right panel, the Madelung energy $-c_1 r_s/2$ has been substracted) for a system of 56 electrons in 56×56 sites. The average was done on 5×10^5 walkers. The empty symbols show the variational results while the full symbols show the FN walking estimates at $\beta=16$ for the hybrid (diamonds), crystal (square), and liquid (circles) GWF. The arrows indicate the evolution from the variational to the FN estimate. $\rho_{\min}$ and $\rho_{\max}$ are measured in a percentage of the average density.

somewhere between the liquid and the crystal results, and the FN results get even closer to the liquid for not too large r_s (roughly $r_s\leqslant 60$). At a basic level, the raw reason why the hybrid GWF allows one to gain energy with respect to (the previously used), crystal GWF is therefore quite simple; electrons in the crystal GWF are far too localized, and the hybrid GWF helps to restore a better balance between kinetic and electrostatic energy.

VI. TECHNICAL ASPECTS

In this section, we address various technical points. We start with some reference values of the energy that can be compared directly with the literature. We proceed with studying the thermodynamic ($N\to\infty$) and continuum ($\nu\to 0$) limit. Then, we determine precisely the critical value $r_s^*\approx 31.5\pm 0.5$ at which the transition between the liquid and the hybrid phase takes place. After discussing the status of the mixed estimators, we end the section with showing that in addition to a upper bound to the energy, a lower bound can also be extracted from the FN-QMC datas.

Comparison with the literature. We start with a discussion of an (almost) square system of 56 particles in 210×208 sites. This system is close to systems previously

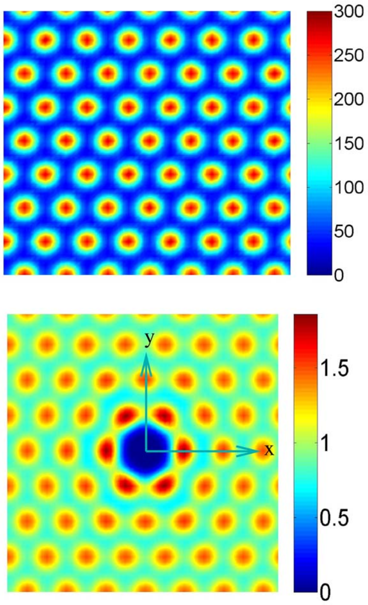

FIG. 9. (Color online) Density $\rho(\vec{r})$ (upper panel) and density-density correlations $g(\vec{r})$ (lower panel) at $r_s=35$ for 56 electrons in 56×56 for the hybrid GWF as a function of $\vec{r}=(x,y)$. The density is plotted in percentage of the average density. Its minimum (maximum) correspond to 35% (230%) of the average density.

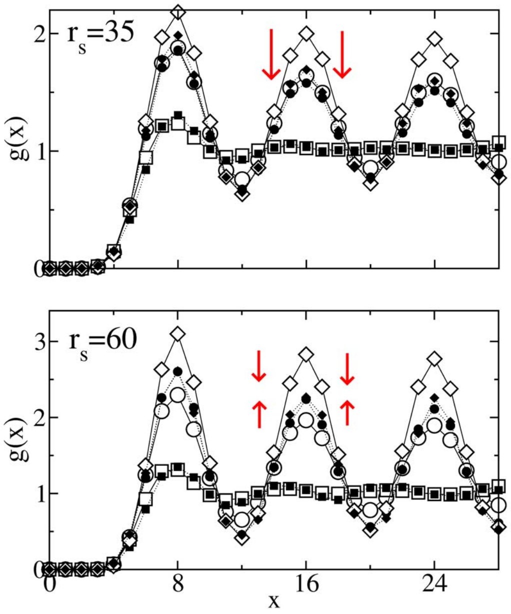

FIG. 10. (Color online) Cross section of $g(\vec{r})$ with $\vec{r}=(x,0)$ as a function of x for 56 electrons in 56×56. The empty (full) symbols are the variational (FN) results, respectively, for the hybrid (circles), crystal (diamonds), and liquid (squares) GWF. The upper (lower) panel corresponds to $r_s=35$ ($r_s=60$). The arrows indicate the direction of the evolution from the variational to the FN estimate while at $r_s=35$ both the crystal and hybrid GWF tends to get delocalized, at $r_s=60$, the peaks of the hybrid GWF get more pronounced after the FN projection.

TABLE I. Selected values of energy for the three GWF as well as values from the literature for comparison. The energies have been averaged over $50/t \leqslant \beta \leqslant 100/t$ and calculated with an average of 25 000 walkers. The statistical error is of the order of 1 in the last digit for our data and is indicated in parentheses for the results of the literature. The parameter A has been optimized at the variational level and is very well fitted by $A \approx 0.59 r_s^{0.57}$ for the liquid and a little lower for the crystal while the liquid values have been used for the hybrid GWF. $U^* = 0.005$ which corresponds to the splitting of the lowest band. The parameter d_0 has also been optimized at the variational level and to a very good approximation $d_0/a \approx (10/r_s)^{1/4}$.

GWF	N	$L_x \times L_y$		$r_s=20$	$r_s=30$	$r_s=35$	$r_s=40$	$r_s=50$	$r_s=60$	$r_s=70$	$r_s=75$
Liquid	56	210×208		−18.499	−28.744	−33.906	−39.097	−49.532	−60.017		
Crystal	56	210×208			−28.728	−33.904	−39.104	−49.558	−60.074	−70.634	
Hybrid	56	210×208	$U^*=0.005$		−28.734	−33.911	−39.113	−49.563	−60.080	−70.640	
Liquid	57	Continuum	Ref. 3		−28.722(4)		−39.073(2)				−75.788(8)
Crystal	56	Continuum	Ref. 3		−28.700(2)		−39.090(4)	−49.526(4)			−75.904(3)
Liquid	57	Continuum	Ref. 6		−28.734(2)		−39.092(3)				−75.825(3)
Crystal	56	Continuum	Ref. 6		−28.730(2)		−39.102(2)	−49.558(3)			−75.918(3)

studied in the literature, and can hence serve as a reference. The absolute values of the FN energies are given in Table I together with the results of Refs. 3,6. The same data (without Ref. 3) are represented in Fig. 11, where we plotted the zero-point motion energy $2[E_{\mathrm{FN}} - c_1 r_s/2]/r_s^{1/2}$ (which converges toward $c_{1/2}$ at $r_s \gg 1$) as a function of r_s. We find a good agreement with the more recent data of Ref. 6 while the original data of Ref. 3 are about ~0.015 higher (Ref. 3 and Ref. 6 used the same numerical code in their calculations). The observed small differences can be due to the following systematic errors: (i) too small $\beta < \beta_{\mathrm{sat}}$. Here we averaged the results over $50 \leqslant \beta \leqslant 100$ and some more energy (0.003) can probably be gained by using higher values of β. Increasing β not only involves more computing time, but also using more walkers to keep the exponential increase of the variance under control. (ii) Small residual effect of the lattice (see Fig. 14 below), (iii) shell effects [Refs. 3 and 6 used 57 particles (complete shell) for the liquid while we used the same $N=56$ system for all three phases. This effect can account for a difference of energy of ~0.004 at $r_s=40$, see Fig. 12 below], and (iv) a finite number of walkers.

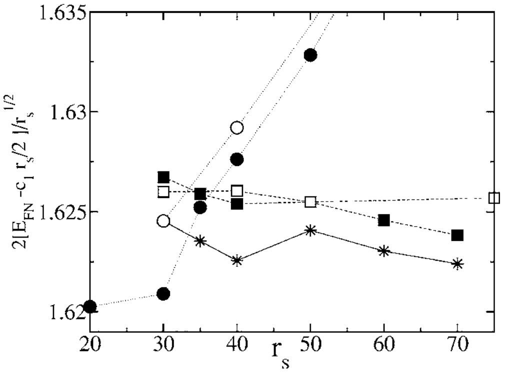

FIG. 11. Comparison with the results of the literature for a system of 56 electrons in 210×208 sites. The plot shows the rescaled energy $2[E_{\mathrm{FN}} - c_1 r_s/2]/r_s^{1/2}$ which converges toward the zero point motion $c_{1/2}$ correction to the energy at high r_s. The symbols correspond to our calculation with the liquid GWF (full circles), solid GWF (full squares), hybrid GWF (stars), and to the calculation of Ref. 6 for the liquid (empty circles, 57 particles) and solid (empty squares).

Thermodynamic ($N \to \infty$) limit. In Fig. 12 we examine the finite N effect for the liquid GWF. Those can be already be understood by looking at the finite N corrections to the energy at $r_s=0$ (see Fig. 13 upper left panel); one finds that the (exact) kinetic energy $E_c(r_s=0,N) = 1 + \Delta E_c(N)$ strongly oscillates with N for small values of N before saturating toward 1. These oscillations correspond to the filling of the various shells of equal energies. Hence, following Ref. 3, we fit the N dependence of the liquid energy with the form,

$$E(N) = E_\infty + E_c(r_s)\Delta E_c(N) - A(r_s)/N. \qquad (17)$$

However, contrary to Ref. 3, we do not let the coefficient $E_c(r_s)$ be a fitting parameter but rather fix it to the calculated kinetic energy [for a given value of N, the finite N corrections to $E_c(r_s)$ are irrelevant at the precision of the calcula-

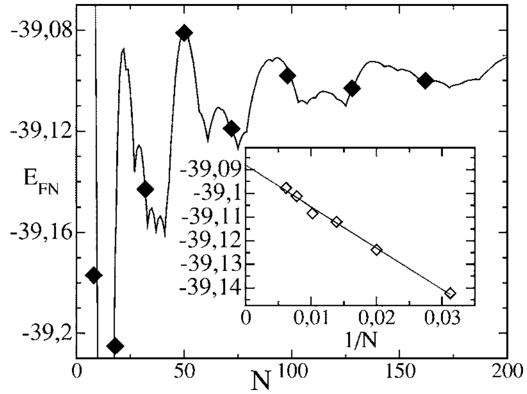

FIG. 12. Finite N effect on the fixed-node energy with the liquid GWF at $r_s=40$. Energy averaged over $25/t \leqslant \beta \leqslant 50/t$ as a function of the number N of particles with $A=4.5$ for a system of $N=2P^2$ particles in $16P \times 28P$ sites ($P=2\cdots 9$ diamonds). The fit (solid line) corresponds to $E=-39.088+E_c^{50}(r_s=40)\Delta E_c(N) - 1.75/N$, where $E_c^{50}(r_s=40)=2.5$ is the (fixed-node) kinetic energy for 50 particles and $\Delta E_c(N)$ is the exact finite size correction to the kinetic energy computed at $r_s=0$. Inset: the oscillatory correction $E_c^{50}(r_s=40)\Delta E_c(N)$ has been subtracted from the energy which is plotted as a function of $1/N$. The solid line is a linear fit to the data $E=-39.088-1.75/N$.

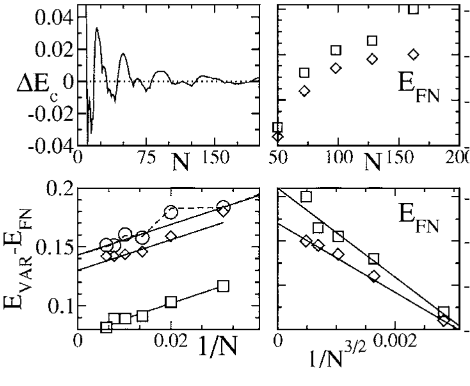

FIG. 13. The finite N effect in a system of $N=2P^2$ particles in $16P \times 28P$ sites. Upper left panel, exact finite size correction $\Delta E_c(N)$ to the liquid kinetic energy at $r_s=0$. This curve is used to remove the oscillatory dependance of the liquid energy due to the shell structure. Lower left panel, difference between the variational and fixed-node energy $E_{\text{VAR}}-E_{\text{FN}}$ as a function of $1/N$ for the liquid (circle, $A=4.5$), hybrid (diamonds, $U^*=0.12$, $A=4.5$), and crystal (square, $d_0/a=0.74$, $A=4$). The linear fits (solid lines) are, respectively, $y=0.143+1.3/N$, $y=0.13+1.3/N$, and $y=0.075+1.3/N$. A better fit is obtained for the liquid using (dashed line) $y=0.143+1.3/N+0.8\Delta E_c(N)$. Right panels, FN energy for the crystal (squares) and hybrid (diamonds, $U^*=0.12$) as a function of N (upper right panel) and $1/N^{3/2}$ (lower right panel). The fits (solid lines) are, respectively, $y=-39.108-10.1/N^{3/2}$ and $y=-39.116-7.8/N^{3/2}$.

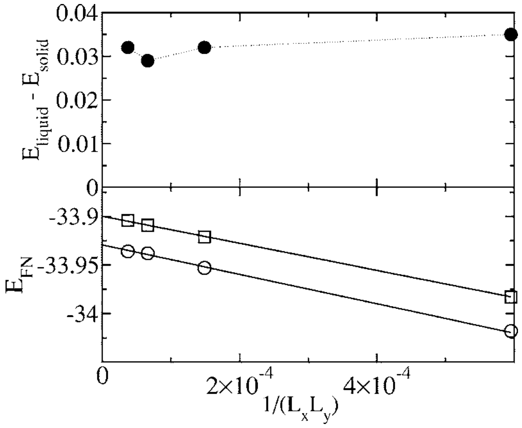

FIG. 14. The effect of dilution on the fixed-node energy for a system of 30 particles in $40P \times 42P$ sites ($P=1$, 2, 3, and 4) at $r_s=35$. Lower panel, the energy of the liquid GWF (circles) and solid GWF (squares, $d_0=0.82$) as a function of the inverse volume $1/(L_xL_y)$. The lines serve as a guide to the eye. Upper panel, the difference of energy between the liquid and the solid GWF as a function of $1/(L_xL_y)$.

tions]. Hence, we plot in the inset of Fig. 12 the liquid energy to which the $E_c(r_s)\Delta E_c(N)$ correction has been substracted, and find a very good agreement with a $1/N$ residual error. The quality of the overall (two parameters) fit can be found in Fig. 12 for up to 162 particles. In the lowest left panel of Fig. 13, we have plotted the difference between the FN and the variational energy as a function of $1/N$ (circles for the liquid). We find that this difference presents some finite N effect about as strong as those of the FN energy alone [here $E_{\text{FN}} \approx -39.088+2.5\Delta E_c(N)-1.75/N$ while $E_{\text{VAR}}-E_{\text{FN}} \approx 0.143+0.8\Delta E_c(N)+1.3/N$]. The difference between the finite N behavior of the variational and FN result is not very surprising since for those intermediate values of r_s (here $r_s=40$), the difference $E_{\text{VAR}}-E_{\text{FN}}$ is about 10 times larger than those effects. The same conclusion also holds for the hybrid (diamond) and crystal (squares) GWF.

The finite N behavior of the crystal and hybrid results are much simpler. They do not present the same oscillatory behavior but rather converge smoothly toward the $N \gg 1$ value (as shown in the upper right panel of Fig. 13). A good fit is obtained by plotting the FN energies as a function of $1/N^{3/2}$ (which is the expected finite effect for the crystal at large r_s). We find that the difference between the crystal and hybrid slightly increases as N gets bigger. (The respective fits are $E_{\text{FN}}=-39.108-10.1/N^{3/2}$ for the crystal GWF and $E_{\text{FN}}=-39.116-7.8/N^{3/2}$ for the hybrid.) We repeated the same procedure at $r_s=50$ (up to 98 particles only) and arrive at a similar result ($E_{\text{FN}}=-49.56-13.8/N^{3/2}$ for the crystal GWF and $E_{\text{FN}}=-49.567-12.2/N^{3/2}$ for the hybrid.)

Continuum ($\nu \to 0$) *limit*. The presence of the underlying lattice can induce a correction to the continuum result. This effect is a small correction however, and should not be mixed-up with the much larger effects that can take place[33,34] at much higher values of r_s. In addition, contrary to the finite N effect which one would like to avoid (since we make use of Ewald resummation, we do not look at mesoscopic samples in this study), there is an underlying lattice in real (semiconductor based) samples. In the lower panel of Fig. 14, we plot the energy as a function of the inverse of the surface of the sample for a fixed number of particles. We find indeed a $1/(L_xL_y)$ correction to the energy. However, (the upper panel in Fig. 14), this correction is almost GWF independent so that the relative stability of the phases is unaffected by the lattice for the $\nu=1/224$ and $\nu=1/780$ samples. For the latter, the correction is almost negligible and we have a quantitative good agreement with the continuum model for the absolute values of the energy (see Fig. 11).

Critical value of r_s. We now determine precisely the critical value r_s^* at which the liquid-hybrid transition takes place (Fig. 15). In the left panel of Fig. 15, we plot the energy of the hybrid and liquid phases as a function of r_s for various (rather small) values of β. For each of them we extract the crossing point $r_s^*(\beta)$ which is plotted in the upper right panel of Fig. 15. We find that $r_s^*(\beta)$ saturates for rather small values of $\beta \approx 2/t$ indicating that the gain in energy obtained by increasing β further ($\beta_{\text{sat}} \approx 25/t$ for this system) is almost GWF independent. The obtained r_s^* is plotted in the lower part of the right panel as a function of the number of particles for several filling factors. At large N, r_s^* converges toward $r_s^*=31.5 \pm 0.5$.

Variational, mixed, and fixed-node estimates. For a given observable O, three different estimates can be constructed. The variational $O_{\text{VAR}}=\langle\Psi_G|O|\Psi_G\rangle$ and the fixed-node (forward walking) estimates $O_{\text{FN}}=\langle\Psi_0^{\text{FN}}|O|\Psi_0^{\text{FN}}\rangle=\langle\Psi_G|e^{-H^{\text{FN}}\beta/2}Oe^{-H^{\text{FN}}\beta/2}|\Psi_G\rangle$ have been used throughout this paper. An intermediate one, the mixed estimate $O_{\text{MX}}=\langle\Psi_G|O|\Psi_0^{\text{FN}}\rangle=\langle\Psi_G|Oe^{-H^{\text{FN}}\beta}|\Psi_G\rangle$ is easy to compute and hence very common in QMC calculations. For most applica-

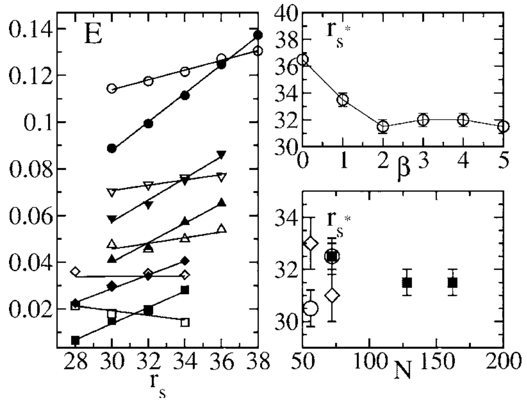

FIG. 15. Determination of the critical value r_s^*. Left panel, energy of the liquid (full symbols) and hybrid (empty symbols) as a function of r_s for $\beta=0,\ 1,\ 2,\ 3$, and $5/t$ (top to bottom) with their corresponding linear fits. The system contains 128 electrons in 128×224 sites and $-c_1r_s/2+c_{1/2}r_s^{1/2}/2$ has been substracted to the energy. Upper right panel, resulting r_s^* (crossing points of the left panel) as a function of β. Lower right panel r_s^* (at $\beta\rightarrow\infty$) as a function of N for a filling factor of $\nu=1/56$ (empty circles), $\nu=1/224$ (full squares), and $\nu=1/780$ (empty diamonds).

tions, $|\Psi_G\rangle$ is a reasonable approximation of the ground state $|\Psi_0^{\mathrm{FN}}\rangle$ so that the mixed results O_{MX} can be extrapolated toward the FN result using the (first-order correction) formula $O_{\mathrm{FN}}\approx2O_{\mathrm{MX}}-O_{\mathrm{VAR}}$. The mixed estimate is much easier to obtain than the FN estimate, since the latter requires one to apply $e^{-H^{\mathrm{FN}}\beta/2}$ after the measurement has been made, and the deaths and births involved in the reconfiguration process considerably decrease the statistics. However, in the range of r_s studied in this paper, we find important differences between the different estimates so that it is necessary to use the FN estimates. To illustrate this point, we plot in Fig. 16 $O_{\mathrm{FN}}(\beta)$ (left panels) and $O_{\mathrm{MX}}(\beta)$ (right panels) for the kinetic energy E_c (upper panels, $E_c\approx1$ at $r_s=0$) and the interaction energy E_{int} (lower panels). For the case considered in Fig. 16, the mixed estimate is a very poor estimate of the true (FN) estimate. Indeed, we have $E_c^{\mathrm{VAR}}\approx2.01$, $E_c^{\mathrm{MX}}(\beta=8)\approx1.97$, and $E_c^{\mathrm{FN}}(\beta=8)\approx2.01$ so that the interpolation from the mixed estimate would be very bad.

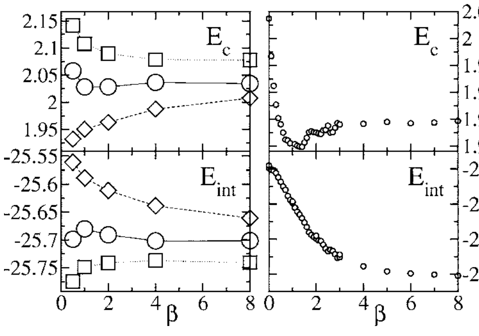

FIG. 16. A comparison of the different estimates of the kinetic and interaction energies for a system of 30 particles in 40×42 sites at $r_s=25$. Left panels, FN estimate for the liquid (diamonds), crystal (squares), and hybrid (circles) GWF. Right panels, mixed estimate for the liquid phase. Upper panels: the kinetic energy $E_c(\beta)$. Lower panels: the interaction energy $E_{\mathrm{int}}(\beta)$.

Lower bound to the total energy. The evolution of the kinetic and interaction energy with β can be put to further use; we find that $E_c^{\mathrm{liq}}(\beta)<E_c^{\mathrm{hyb}}(\beta)<E_c^{\mathrm{cry}}(\beta)$ while $E_{\mathrm{int}}^{\mathrm{cry}}(\beta)<E_{\mathrm{int}}^{\mathrm{hyb}}(\beta)<E_{\mathrm{int}}^{\mathrm{liq}}(\beta)$ (consistent with the interpretation that the hybrid phase is intermediate between the liquid and the crystal). As both $E_c^{\mathrm{liq}}(\beta)$ and $E_{\mathrm{int}}^{\mathrm{cry}}(\beta)$ increases with β, (and since by construction the liquid and crystal GWF favor, respectively, the kinetic and interaction energy), we conjecture that they form true *lower bounds* of the kinetic and interaction energies of the true ground state of the system. Hence, in addition to an upper bound of the total energy, we can also construct a lower bound,

$$E_c^{\mathrm{liq}}+E_{\mathrm{int}}^{\mathrm{cry}}\leqslant E_0\leqslant E_{\mathrm{FN}}^{\mathrm{hyb}}, \tag{18}$$

which for the case of Fig. 16 gives $-23.73\leqslant E_0\leqslant-23.67$ with a precision of 0.3%. This lower bound is of interest to us, as it allows one to estimate that the gain in energy provided by the hybrid GWF (with respect to the crystal and liquid one) is a significant fraction of the distance to the lower bond.

VII. DISCUSSION

We conclude this paper with a discussion of several topics linked with the present study. Indeed, once we have established that for intermediate r_s, the system behaves neither as liquid nor as crystal, the need to discriminate between the various possible candidates for the intermediate phase remains. Below follows a short discussion of some of those proposals. To go beyond and establish, for instance, the presence or the absence of orientational and translational order, one would need a finite-size study of the correlations funcions and one way or another to release the fixed-node constraint. These much needed extensions should be the subject of future works.

Spin of the electrons. We restricted the present study to fully spin-polarized electrons. Indeed, as the interaction energy gets bigger, the system can minimize its interaction energy by antisymmetrizing the orbital part of its wave function, and it was found (for instance in Refs. 6 and 7) that above $r_s\geqslant20$ (which is the range of our study) the polarized liquid is more stable than the unpolarized one. A strong inplane magnetic field would also polarize the system at a smaller value of r_s.

Multiple exchange. At high r_s when the crystal is well established, a multiple exchange (of two, three, or more particles) can take place,[35] leading to an effective interaction between the electronic spins. Recently these exchange interactions were estimated using the (finite temperature) path integral QMC technique.[10,36] The authors proposed that the melting of the crystal is actually due to a divergence of a multispin exchange. In those calculations, some sort of FN approximation was used below $r_s\approx60$ to stabilize the crystal. Summing up the exchange energies calculated in,[10] we find (in our unit) $E_{\mathrm{ex}}\approx0.001$ at $r_s=50$ (where the calculation is most robust). This energy is relatively small and cannot account for the difference observed between the hybrid and crystal GWF results. The difference between these path integral calculations and those presented in this paper lies in the FN approximation (the one used in Ref. 10 seems to stabilize a well-localized crystal) and the use of a rather large temperature $T \approx 0.08$ (which is roughly three times bigger than the energy difference between the crystal and the liquid at $r_s = 50$ and 100 times bigger than the calculated exchange energies).

Hexatic and supersolid phase. Among the proposed intermediate phases is the presence of a hexatic quantum phase in between the liquid and the crystal.[15,16] Such a phase would have orientational order, but no translational order. The hybrid GWF is made of Bloch waves that have, by construction, a hexagonal Fermi surface (one full band corresponds to the momentum in the first Brillouin zone of the triangular crystal). However, we have also explicitly broken the translational symmetry so that, at the variational level, the hybrid GWF certainly does not correspond to a hexatic phase. Upon applying the FN projection operator, the translational symmetry tends to be restored (see the left panels of Fig. 8, for instance) so that the present calculations cannot rule out the possibility of a quantum hexatic phase. Another proposition is the presence of a supersolid phase,[20–22] i.e., the quantum coexistence of a liquid (of delocalized defects for instance) with the crystal. Qualitatively, the hybrid phase is in agreement with the idea of the supersolid phase as discussed in Ref. 37. In the supersolid phase described in Ref. 19 however, one expects the number of electrons in the crystal to be smaller than the total number of electrons. We tried to construct such a GWF without success.

Bubbles and stripes. Around the melting point of a classical liquid-solid phase transition, the system gains some energy by being in a coexistence of the two phases. In the present system such a macroscopic phase separation is not possible since it would lead to a macroscopic dipole. Spivak and Kivelson recently proposed that a series of microemulsion phases (bubbles/stripes of solid/liquid in the liquid/solid) can however, take place.[17,18] If they exist, these microemulsions take place between the two values of densities n_s and n_l (in electrons per bohr radius squared) that come out of the Maxwell construction, $\partial_n E^{\mathrm{sol}}(n_s) = \partial_n E^{\mathrm{liq}}(n_l) = [E^{\mathrm{liq}}(n_l) - E^{\mathrm{sol}}(n_s)]/(n_l - n_s)$ (energies in Rydberg). Solving for n_s and n_l using the FN energies, we find that the (maximum) range of r_s, where these microemulsions could occur is $|r_s - r_s^*| \leqslant \Delta r_s$ with $\Delta r_s \approx 0.04$ [r_s^* is the transition point. To a good approximation, $\Delta r_s \approx r_s^* \alpha / c_1$, where the change of slope $\alpha \approx 0.003$, defined as $E^{\mathrm{liq}} \approx E^{\mathrm{sol}} + \alpha(r_s - r_s^*)$ around the transition can be extracted from Fig. 1 or Fig. 15]. The argument was originally developed for the liquid/crystal transition but holds equally well for the liquid/hybrid transition described in this paper (a direct liquid/crystal transition would lead to $\Delta r_s \approx 0.06$). The maximum gain of energy given by the Maxwell construction (which uses the energies calculated for *neutral* phases, hence only a fraction of this energy can possibly be gained by microemulsions) is $\Delta E \approx 2\alpha^2/(c_1 r_s^*) \approx 0.2\ \mu\mathrm{Ry}$ ($\approx 10^{-4}$ in our units).

Metal insulator transition. About 10 years ago, an interest in two-dimensional systems arose from the work of Kravchenko *et al.*[38] who reported on an unexpected metal-insulator transition. It was followed by an important body of literature but the origin of this transition is still under debate.[39–41] The problem involves understanding the role of disorder in the system and lies outside the scope of this paper. Indeed the effect of disorder is a complicated issue and depends not only on the strength of the disorder but also on the typical length scale on which the potential varies. For instance, the component of the disorder varying on the scale of the interelectron distance is likely to pin and stabilize a crystal (or glassy) phase. A disordered potential varying on a larger length scale however, will favor fluctuations of the density and hence phase separation. In actual samples, long length scale fluctuations have been observed using local compressibility measurements.[42]

A natural question for us is whether puddles of hybrid/crystal phase are actually present in the experiments. As the mobility of the two-dimensional systems improved in the past years, so had the critical value of r_s, where the transition is observed. In whole GaAs devices it goes from (Refs. 42 and 43) $r_s = 20-25$ to (Refs. 44 and 45) $r_s \approx 55-60$ in the cleanest samples, i.e., well above $r_s^* = 31.5$. At $r_s = 60$, the difference of energy between the liquid and the crystal phase is roughly 0.03 mRy per particle (see the lower panel of Fig. 1) so that the melting temperature of the crystal should be slightly larger (the crystal should be stabilized by its spin entropy through the Pomeranchuk effect[20]) which translates into temperatures of a few tens of mK. Those temperatures are therefore within the possibilities of a good dilution fridge though slightly below the temperatures that are usually studied.

Conclusion: How liquid is the hybrid phase? To summarize the main message of this paper, we find that in these intermediate regions of densities, where little of the physics is known, the fixed-node quantum Monte Carlo technique should be viewed as a probe. The freedom in the choice of the GWF allows one to start with a GWF that captures some sort of physics (as seen in the variational calculation) and the evolution of the various (not only the energy) physical quantities upon applying the fixed-node projection operator giving us insights on the physics of the true ground state. In short, one introduces physics in a GWF and sees whether this physics is stabilized or washed out by the FN-QMC algorithm.

With this paradigm in mind, we followed the evolution (from variational to FN) of the physical quantities available within our algorithm. For $31.5 \leqslant r_s \leqslant 60$, we found that all show the same tendency to delocalization. The success of the hybrid GWF, with respect to the crystal one, is associated to its (much more) delocalized nature that allow a better balance between kinetic and electrostatic energy. The success of the hybrid GWF with respect to the liquid one, however, is associated to the change in symmetry as the hybrid GWF is constructed out of delocalized waves. We conclude that while the nature of the ground state above $r_s^* = 31.5$ might still not be fully elucidated, the fact that it is not a liquid, yet not a localized crystal is now put on very firm ground. At large r_s the system eventually gets localized. At the present we cannot say whether this occurs through a crossover or a second transition.

ACKNOWLEDGMENT

It is a pleasure to thank B. Bernu, M. Holzmann, D. L'Hôtes, J. Houdayer, O. Parcollet, F. Portier, J-L. Pichard, P. Roche, and B. Spivak for very interesting discussions and comments. Special thanks to Houman Falakshahi with whom this work was initiated.

---

[1] D. Pines and P. Nozieres, *Theory of Quantum Liquids* (Benjamin, New York, 1966).
[2] E. P. Wigner, Phys. Rev. **46**, 1002 (1934).
[3] B. Tanatar and D. M. Ceperley, Phys. Rev. B **39**, 5005 (1989).
[4] M. Imada and M. Takahashi, J. Phys. Soc. Jpn. **53**, 3770 (1984).
[5] W. M. C. Foulkes, L. Mitas, R. J. Needs, and G. Rajagopal, Rev. Mod. Phys. **73**, 33 (2001).
[6] F. Rapisarda and G. Senatore, Aust. J. Phys. **49**, 161 (1996).
[7] C. Attaccalite, S. Moroni, P. Gori-Giorgi, and G. B. Bachelet, Phys. Rev. Lett. **88**, 256601 (2002).
[8] Y. Kwon, D. M. Ceperley, and R. M. Martin, Phys. Rev. B **48**, 12037 (1993).
[9] S. De Palo, S. Conti, and S. Moroni, Phys. Rev. B **69**, 035109 (2004).
[10] B. Bernu and D. M. Ceperley, cond-mat/0310309 (unpublished).
[11] E. Y. Andrei, G. Deville, D. C. Glattli, F. I. B. Williams, E. Paris, and B. Etienne, Phys. Rev. Lett. **60**, 2765 (1988).
[12] J. M. Kosterlitz and D. J. Thouless, J. Phys. C **6**, 1181 (1973).
[13] P. M. Platzman and H. Fukuyama, Phys. Rev. B **10**, 3150 (1974).
[14] B. I. Halperin and D. R. Nelson, Phys. Rev. Lett. **41**, 121 (1978).
[15] V. Oganesyan, S. A. Kivelson, and E. Fradkin, Phys. Rev. B **64**, 195109 (2001).
[16] D. G. Barci and L. E. Oxman, Phys. Rev. B **67**, 205108 (2003).
[17] R. Jamei, S. Kivelson, and B. Spivak, Phys. Rev. Lett. **94**, 056805 (2005).
[18] B. Spivak and S. A. Kivelson, Phys. Rev. B **70**, 155114 (2004).
[19] A. F. Andreev and I. M. Lifshitz, Sov. Phys. JETP **29**, 1107 (1969).
[20] B. Spivak, Phys. Rev. B **67**, 125205 (2003).
[21] G. Katomeris, F. Selva, and J-L. Pichard, Eur. Phys. J. B **31**, 401 (2003).
[22] Z. A. Nemeth, and J-L. Pichard, Eur. Phys. J. B **33**, 87 (2003).
[23] I. Nagy, Phys. Rev. B **60**, 4404 (1999).
[24] H. Falakshahi and X. Waintal, Phys. Rev. Lett. **94**, 046801 (2005).
[25] D. F. B. tenHaaf, H. J. M. vanBemmel, J. M. J. vanLeeuwen, W. vanSaarlos, and D. M. Ceperley, Phys. Rev. B **51**, 13039 (1995).
[26] N. Trivedi and D. M. Ceperley, Phys. Rev. B **41**, 4552 (1990).
[27] D. Ceperley and G. V. Chester, Phys. Rev. B **16**, 3081 (1977).
[28] S. Sorella, Phys. Rev. Lett. **80**, 4558 (1998).
[29] M. Tinkham, *Introduction to Superconductivity* (McGraw-Hill, New York, 1975).
[30] F. A. Stevens, Jr. and M. A. Pokrant, Phys. Rev. A **8**, 990 (1973).
[31] W. Kohn, Phys. Rev. **115**, 809 (1959).
[32] E. I. Blount, *Solid State Physics* (Academic Press), New York, 1962).
[33] H. Falakshahi, Z. Németh, and J.-L. Pichard, Eur. Phys. J. B **39**, 93 (2004).
[34] Z. A. Nemeth and J-L. Pichard, Eur. Phys. J. B **45**, 111 (2005).
[35] M. Roger, Phys. Rev. B **30**, 6432 (1984).
[36] B. Bernu, L. Candido, and D. M. Ceperley, Phys. Rev. Lett. **86**, 870 (2001).
[37] A. J. Leggett, Phys. Rev. Lett. **25**, 1543 (1970).
[38] S. V. Kravchenko, G. V. Kravchenko, J. E. Furneaux, V. M. Pudalov, and M. D'Iorio, Phys. Rev. B **50**, 8039 (1994).
[39] E. Abrahams, S. V. Kravchenko, and M. P. Sarachik, Rev. Mod. Phys. **73**, 251 (2001).
[40] S. V. Kravchenko and M. P. Sarachik, Rep. Prog. Phys. **67**, 1 (2004).
[41] V. M. Pudalov, condmat/0405315 (unpublished).
[42] S. Ilani, A. Yacoby, D. Mahalu, and H. Shtrikman, Science **292**, 1354 (2001).
[43] R. Leturcq, D. L'Hote, R. Tourbot, C. J. Mellor, and M. Henini, Phys. Rev. Lett. **90**, 076402 (2003).
[44] H. Noh, M. P. Lilly, D. C. Tsui, J. A. Simmons, E. H. Hwang, S. DasSarma, L. N. Pfeiffer, and K. W. West, Phys. Rev. B **68**, 165308 (2003).
[45] H. Noh, M. P. Lilly, D. C. Tsui, J. A. Simmons, L. N. Pfeiffer, and K. W. West, Phys. Rev. B **68**, 241308(R) (2003).